ARTICLE

Carbonyl-Induced Reduction from Co(III) to Co(II) in Co_xS_y Enables Sulfate Radical-Dominated Peroxymonosulfate Activation

Liyuan Wu[a, b, *], Chaoyang Wang[a, b], Xin Wang[c], Xun Zhang[a, b], Qian Yu[a, b], Yuanyuan Jiang[a, b], Kaiyu Chen[a, b], Wenli Yang[a, b], Pengpeng Guo[d, *], Haiyan Li[a]

Received
Accepted

DOI:

Cobalt sulfide (Co_xS_y) shows promise for activating peroxymonosulfate (PMS) in advanced oxidation processes (AOPs), but its application faces key challenges, including low sulfate radical ($SO_4^{\bullet-}$) generation, inefficient PMS decomposition, and limited mineralization efficiency for antibiotic removal. This study addresses these limitations by coordinating carbonyl groups (C=O) with cobalt to stabilize low-valence cobalt species and enhance electron transfer through defect engineering. A lignite-activated coke-supported cobalt sulfide (LAC@Co_xS_y-V) was synthesized, exhibiting a nearly complete conversion to low-valence cobalt (Co^{2+}) and abundant sulfur vacancies. Compared to Co_xS_y/PMS system, the K_{obs} of sulfamethoxazole (SMX) degradation and the mineralization efficiency of SMX in the LAC@Co_xS_y-V/PMS system are 18-fold and 2-fold higher, respectively. Mechanistic studies revealed that Co_xS_y complexed on the LAC surface enables cobalt-carbonyl coordination, facilitating electron transfer from the electronegative O in the carbonyl groups to Co^{3+}, reducing it to Co^{2+}. The introduction of sulfur vacancies further increases the proportion of low-valence cobalt, promoting PMS activation to generate $SO_4^{\bullet-}$. These radicals act as the primary reactive oxygen species (ROS), while sulfur vacancies simultaneously promote singlet oxygen ($^1O_2$) generation, synergistically enhancing SMX degradation. The applicability of this system was validated under various conditions, including matrix interference tests, cyclic stability assessment, and continuous-flow fixed-bed reactor experiments simulating medical wastewater treatment. This study provides valuable insight into defect and ligand engineering strategies for efficient antibiotic removal via PMS-AOPs.

Keywords

Peroxymonosulfate; Cobalt sulfides; Sulfur vacancies; Carbonyl group

a Beijing Engineering Research Center of Sustainable Urban Sewage System Construction and Risk Control, Beijing University of Civil Engineering and Architecture, Beijing 100044, China
b Key Laboratory of Urban Stormwater System and Water Environment (Beijing University of Civil Engineering and Architecture), Ministry of Education, Beijing 100044, China
c CNNC Geological Dadi Ecological Technology Co., Ltd., Beijing 100010, China
d Helmholtz-Center for Environmental Research-UFZ, Department Technical Biogeochemistry, Permoserstr. 15, Leipzig 04318, Germany.

ARTICLE

1 Introduction

Sulfamethoxazole (SMX) is one of the most commonly used sulfonamide antibiotics for treating susceptible bacteria[1]. However, due to excessive use and improper disposal, SMX was frequently detectable in various water bodies, with the detection levels ranging from 2-630 ng/L. The residual SMX in the environment has low biodegradability and high persistence, which poses great threats to the ecosystems and humans[2]. Thus, there is an urgent need to develop effective technologies for removing SMX from water circumstances.

Sulfate radical based advanced oxidation processes (SR-AOPs) are uniquely advantageous for the removal of refractory antibiotic pollutants, utilizing highly reactive oxygen species (ROS) such as $SO_4^{\bullet-}$, $^{\bullet}OH$, and $^1O_2$ in PMS activation[3, 4]. The methods of PMS activation are various. Compared with light, heat, and electricity activation methods, heterogeneous activation without external energy input is recognized for its advantages, such as high reactivity, easy operation and recyclability[5]. In previous studies, the Co_xS_y/PMS systems, with $^1O_2$ as the main ROS, have achieved satisfactory degradation performance for SMX[6-8]. In fact, $SO_4^{\bullet-}$ shows stronger reactivity with SMX compared to $^1O_2$ ($k(SO_4^{\bullet-}, SMX) = 1.61 \times 10^{10}$ $M^{-1}s^{-1}$, $k(^1O_2, SMX) = 2 \times 10^4$ $M^{-1}s^{-1}$)[9], and it is also an undeniable fact that $SO_4^{\bullet-}$ displays a higher redox potential ($SO_4^{\bullet-}$: 2.5~3.2 eV; $^1O_2$: 2.2 V) and a longer half-life ($SO_4^{\bullet-}$: 30~40 μs; $^1O_2$: ~4 μs)[10, 11]. Therefore, considering the high-efficiency decomposition and deep mineralization of SMX, constructing a Co_xS_y/PMS system with $SO_4^{\bullet-}$ as the dominant ROS would be an effective and potential technology.

Furthermore, synthesizing Co_xS_y catalyst with a high proportion of low-valence cobalt is anticipated to enhance $SO_4^{\bullet-}$ production, as extensive research has demonstrated the pathway of low-valence transition metal ions reacting with HSO_5^- to readily generate $SO_4^{\bullet-}$[3, 12, 13]. However, this process is usually limited by insignificant electron transfer and the redox of Co^{3+}/Co^{2+}. It is reported that the carboxyl group (C=O) can serve as an electron donor to lower the metal oxidation state during the bonding process between C=O and transition metals[14-16]. The carbonyl oxygen atoms in the carbonous species can coordinate with cobalt atoms, enhancing the electron transfer during the catalytic process. Besides, the creation of sulfur vacancies can also generate low-coordinate metal sites. Due to the absence of S or C atoms, their electron bonding environment was tuned[17-19]. Consequently, the purpose of this study is to prepare a Co_xS_y-based composite material with a high proportion of low-valence cobalt by C=O modification and regulating vacancies, which are adopted to improve the utilization efficiency of PMS and $SO_4^{\bullet-}$ production, thereby SMX elimination and mineralization. Herein, Lignite-activated coke (LAC), enriched with alkaline oxygen-functional groups such as C=O, C=C, etc. is an advisable choice for purposefully modifying cobalt sulfide catalysts[20, 21]. In addition, the grinding method is accustomed to being used for vacancy regulation on account of its simplicity[22].

Herein, a composite material named LAC@Co_xS_y-V with vacancies was prepared for PMS activation towards SMX degradation. The morphology, crystal structure, and chemical element distribution were determined by multiple characterization methods. The operating parameters and the SMX removal efficiency were evaluated and optimized. Besides, the mechanism of strengthening the PMS-$SO_4^{\bullet-}$ decomposition efficiency and the degradation pathway of SMX were revealed. Finally, the practical potential of this composite was explored by column experiments on the coexistence of natural water substances, cycling stability, and COD removal in the simulated medical wastewater treatment system.

2. Materials and methods

2.1 Chemicals

The information of experimental chemicals is placed in the Supporting Information Text S1.

2.2 Analytical method

The methods of contaminant testing and characterization methods are described in the Supporting Information Text S2.

2.3 Synthesis of LAC@CoxSy-V composite material

(1) LAC purification

A certain amount of washed LAC was dispersed in the 5 M HCl solution and soaked for 24 h. It was then rinsed several times with deionized water until neutral, and dried at 80 °C for 12 h. After grinding evenly, the purified LAC was obtained, named HCl-LAC.

(2) Synthesis of Co_xS_y, LAC@Co_xS_y and LAC@Co_xS_y-V.

0.15 g of HCl-LAC was dispersed evenly in 30 ml of deionized water. Then, 0.2 mM (0.582 g) $Co(NO_3)_2{\cdot}6H_2O$ was added to the suspension and ultrasonicated for 20 minutes to ensure thorough mixing. Afterward, 0.2 mM (0.242 g) L-cysteine was slowly added dropwise to the mixture, followed by vigorous stirring and ultrasonication for 30 minutes. The reaction solution was then transferred into a Teflon-lined stainless autoclave and heated at 180 ℃ for 13 h. After cooling to room temperature, the precipitate was collected and washed three times with deionized water and ethanol, respectively. The washed precipitate was then dried in a vacuum freeze dryer for 8 h, and the resulting product was named LAC@Co_xS_y. Simultaneously, Co_xS_y was synthesized using a similar procedure.

$LAC@Co_xS_y$ was subjected to 20-minute uniform grinding for the synthesis of composite material with sulfur vacancies, denoted as $LAC@Co_xS_y$-V.

2.4 Batch experiment procedure

All experiments were carried out in a 250 mL glass beaker with 100 mL contaminated solution under magnetic stirring (400 r/min) at room temperature. Afterward, 1 mg of catalyst was added to the solution and evenly dispersed. A certain amount of PMS was added to the suspension to start the reaction. During the catalytic degradation period, 0.5 mL of the solution sample was withdrawn from the reaction system at different intervals, quenched with 0.5 mL anhydrous ethanol, and filtered through a 0.22 μm polytetrafluoroethylene (PTFE) membrane (JINTENG, China), then quickly detected. The batch experiments were duplicated three times, and the average value and standard deviation were plotted.

3 Results and Discussion

3.1 Characterization of the as-prepared materials

The crystal structure was analyzed by XRD pattern. In Fig.1a, the XRD pattern of HCl-LAC showed two wide diffraction peaks at 2θ of 24.32° and 42.90°, corresponding to (002) and (100) crystal plane reflections of graphitic carbon (JCPDS No. 99-0057). The XRD pattern of Co_xS_y, $LAC@Co_xS_y$, and $LAC@Co_xS_y$-V were shown in Fig.1b. For Co_xS_y, the diffraction peaks centered at 30.52°, 35.13°, 46.78°, and 62.33° were in good agreement with (100), (101), (102) and (103) crystal faces of carollite-structured $Co_{1-x}S$ (JCPDS No 42-0826). And peaks were at 32.42° and 54.94°, corresponding to (200) and (311) crystal surfaces of CoS_2 (JCPDS NO 41-1471). It showed that Co_xS_y has a regular structure and better crystallization. For $LAC@Co_xS_y$, the diffraction peaks at 2θ of 26.60° and 44.27° matched well with (002) and (100) planes of graphite carbon (JCPDS No. 99-0057), and the characteristic (220), (400), (422), (511), (440) and (531) peaks at 27.07°, 38.45°, 47.63°, 50.68°, 55.70° and 58.19° could be indexed to the monoclinic phase of Co_3S_4 (JCPDS No 02-0825), which illustrated Co_xS_y was successfully loaded on LAC surface. However, the crystal phases of Co_xS_y in $LAC@Co_xS_y$ is various, but the intensity of diffraction peaks are weakened, and generated more Co_3S_4 structures. The above phenomenon may be due to the abundant reducing functional groups on the LAC surface, which transferred electrons to the cobalt, then formed into a low-valence state[23]. $LAC@Co_xS_y$-V diffraction peaks strength is reduced, owing to the grinding process causing the crystal structure to produce more vacancies[24].

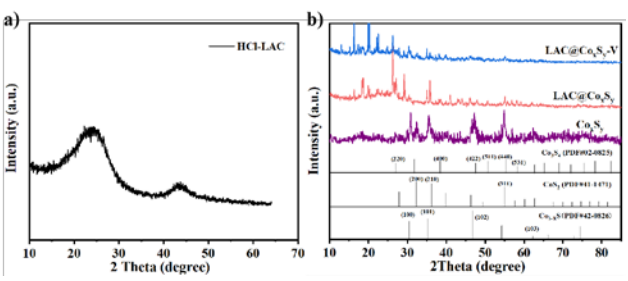

Fig. 1. XRD pattern of (a) HCl-LAC, (b) Co_xS_y, $LAC@Co_xS_y$ and $LAC@Co_xS_y$-V

The SEM images of Co_xS_y, LAC, and $LAC@Co_xS_y$ were shown in Fig.2a~c, respectively. It can be observed that the Co_xS_y was formed by the aggregation of sheet-like structures into spherical clusters, and $LAC@Co_xS_y$ clearly showed that the ball-shaped structure of the Co_xS_y was scattered on the porous LAC particles. In addition, simultaneous distribution of C, Co, and S can be observed in Energy Dispersive X-Ray Spectroscopy (EDX) (as Table S2).

Fig. 2d shows HRTEM image of the pristine Co_xS_y and $LAC@Co_xS_y$, which further confirmed the presence of various Co_xS_y crystal phases and the successful synthesis of $LAC@Co_xS_y$ composite. Among these, the lattice fringes of 0.2522 nm and 0.1788 nm are corresponded to (100) and (102) planes of Co_{1-x} and 0.1820 nm and 0.1980 nm are matched with (200) and (311) planes of CoS_2, respectively. Regarding $LAC@Co_xS_y$-V as Fig.2e, the lattice fringes with the interspacing of 0.1547 nm, 0.2140 nm, 0.2653 nm, 0.2705 nm, and 0.3016 nm suggested the existence of Co_3S_4, corresponding to the facets of (220), (400), (422), (511) and (440) plane. Compared to Co_xS_y, the valence of cobalt in $LAC@Co_xS_y$-V was transformed to a low-valence state, which is favorable for electron transfer. Furthermore, the $LAC@Co_xS_y$-V image displays locally connected nanochannels (green circle), formed by the bending and disordering of LAC after cobalt sulfurization[25]. The above analysis demonstrates that the $LAC@Co_xS_y$-V is successfully obtained. Meanwhile, there are partial lattices of the $LAC@Co_xS_y$-V surface stripes disorderly and unclear, dispersion of the interval black spots (blue circle) may result from the formation of vacancies[26].

To qualitatively analyze these vacancies, the EPR tests were performed (Fig. 2f). The symmetrical signal at g = 2.002 indicated the presence of S vacancies in Co_xS_y, $LAC@Co_xS_y$, and $LAC@Co_xS_y$-V, which agreed with the reported results[27]. Obviously, the signal of $LAC@Co_xS_y$-V is much stronger than those of Co_xS_y and $LAC@Co_xS_y$, implying that S vacancies are newly introduced in $LAC@Co_xS_y$-V after the grinding process. And the EPR spectrum of $LAC@Co_xS_y$ is almost identical to that of pristine Co_xS_y, suggesting the composite processing cannot lead to the introduction of S vacancies in Co_xS_y rather after a grinding process.

XPS was employed to further analyze the near-surface elemental proportions and chemical states of the as-prepared materials. The C 1s high-resolution spectrum of LAC (Fig. 3a) can be divided into four peaks with binding energies at 284.8 eV, 285.8 eV, 288.1 eV, and 291.2 eV, corresponding to C=C, C-O, C=O and π-π* transition[28], respectively. Abundant unsaturated functional groups on the surface of LAC can improve the electron transfer during the reaction[23]. As shown in Table S3, the content of C-O in $LAC@Co_xS_y$ is slightly decreased and shifted to the high energy direction (286.2 eV) compared to LAC, which indicates the formation of C-S bond[21]. Similarly, the content of C=O in $LAC@Co_xS_y$ is slightly reduced and the fitted peak position was offset (288.7 eV), which could be interpreted as chemical interaction between C=O and Co_xS_y.

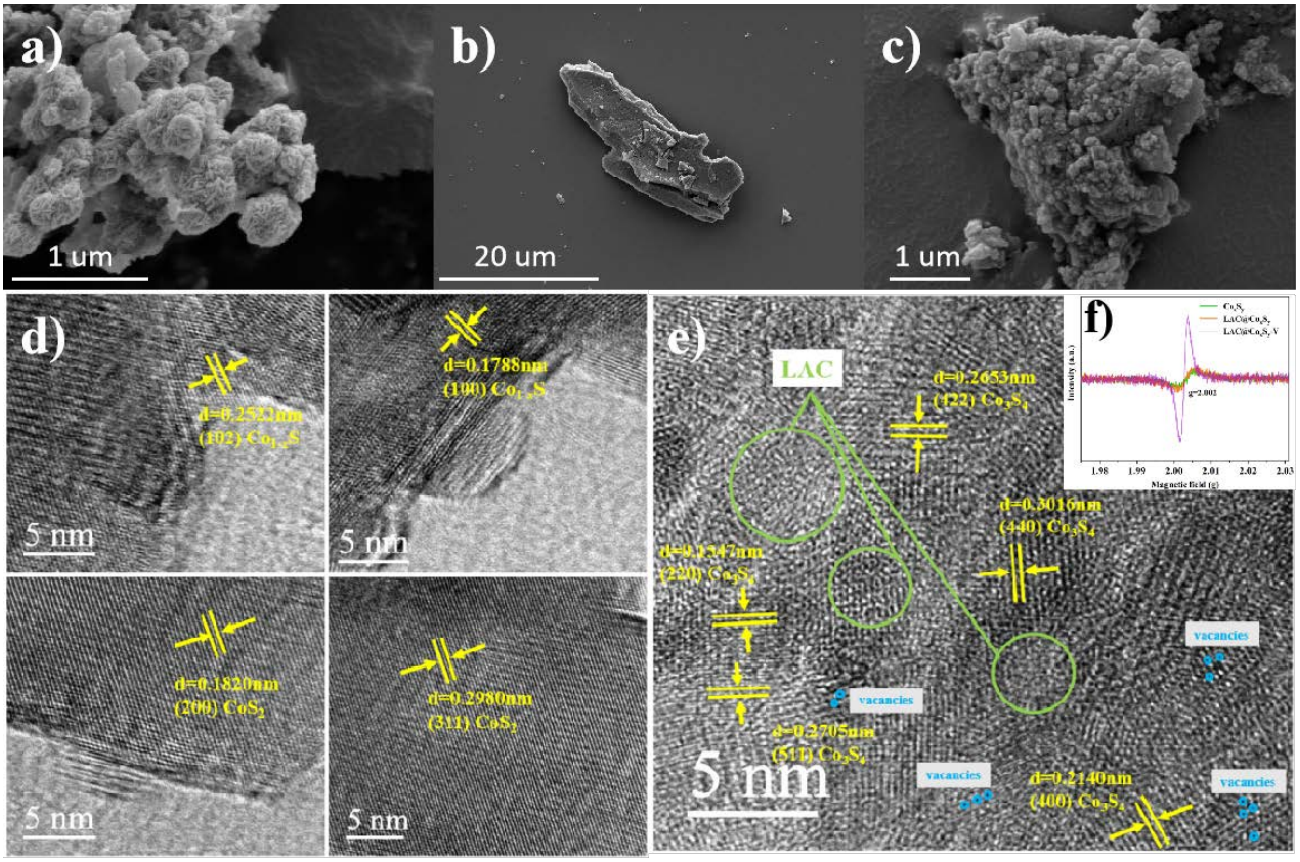

Fig. 2. SEM images of (a) Co_xS_y, (b) LAC, and (c) LAC@Co_xS_y -V; and HRTEM images of (d) Co_xS_y and (e) LAC@Co_xS_y-V. (f) The EPR spectra of sulfur vacancies in Co_xS_y, LAC@Co_xS_y, and LAC@Co_xS_y-V.

Fig. 3b and Table S4 exhibits the high resolution of Co 2p of Co_xS_y, LAC@Co_xS_y and LAC@Co_xS_y-V, which was also fitted with two spin-orbit doublets, Co $2p_{1/2}$ (Co^{2+} at 797.4 eV and Co^{3+} at 793.6 eV) and Co $2p_{3/2}$ (Co^{2+} at 781.8 eV and Co^{3+} at 778.6 eV), and two shake-up satellites (785.5 eV and 803.3 eV)[29]. The fitted peak of Co^{2+} in LAC@Co_xS_y has increased significantly compared with single Co_xS_y, specifically, the proportion increased from 54.55% to 91.32%. And the fitted peak at 797.4 eV slightly shifts to 798.1 eV. This may show the interaction of Co^{2+} and C=O bond. Combined with the changes observed in the C=O peak of the C 1s fitting spectrum, the significant increase in low-valence cobalt indicates that the C=O groups transfer electrons to Co^{3+}. These findings are consistent with the XRD and HRTEM results. Additionally, the Co 2p fitting spectrum shows that the grinding treatment further increases the Co^{2+} content to nearly 100%, likely due to the abundant sulfur vacancies in LAC@Co_xS_y-V[18, 30], although trace Co^{3+} may still remain due to the Co_3S_4 phase observed by XRD.

The S 2p spectrum is shown in Fig. 3c, the binding energy of the S $2p_{3/2}$ and S $2p_{1/2}$ peaks appears at 161.4 eV and 162.6 eV, indicating that most of the S species exist as S^{2-}. The peaks at 163.2 eV and 164.7 eV are attributed to S_2^{2-}. And the peak at 163.9 eV is corresponded to typical C-S bonding, while the peaks at 168.1-169.1 eV are fitted to SO_x^{2-}[31]. The appearance of C-S in LAC@Co_xS_y compared with Co_xS_y indicates that LAC and Co_xS_y composited through chemical interaction.

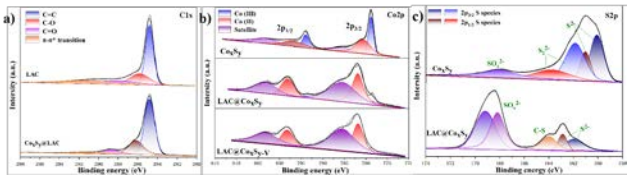

Fig. 3. The XPS spectras of (a) C 1s, (b) Co 2p and (c) S 2p

The FTIR spectrum of LAC, Co_xS_y, LAC@Co_xS_y, and LAC@Co_xS_y-V is shown in Fig. S1. The broadband centered on ~ 3448.7 cm^{-1} is corresponded to the stretch of -OH vibration. The peaks at ~2860.1 cm^{-1} and ~2922.5 cm^{-1} indicate the symmetry and asymmetric stretch of C-H bonds[32]. And the peak at 1083.1 cm^{-1} suggests the existence of C-O group. The peak at ~1656.9 cm^{-1} in LAC is ascribed to C=O stretching vibration[32]. It shows a slight red shift from ~1656.9 cm^{-1} to ~1633.4 cm^{-1} after CoxSy loading, which can be attributed to the electron-withdrawing inductive effect on the carbonyl group induced by the high-valent cobalt species.

The presence of the LAC skeletal vibration (~1555.9 cm^{-1}) and the characteristic metal sulfide stretching bands (~878.7 and ~626.0 cm^{-1}) in the FTIR spectrum of LAC@CoxSy-V provides an evidence for the successful anchoring of Co_xS_y onto the LAC surface[33]. According to XPS analysis, the above phenomenon could be interpreted as an interaction between C and S during the LAC and Co_xS_y combination, which forms C-S bands. In addition, the C=O groups also participate in the response during the composite process. In summary, the

above analysis suggests that the combination of LAC and Co_xS_y is not a single physical process, but a chemical interaction.

3.2 The degradation of SMX by PMS/LAC@Co_xS_y-V.

To explore the catalytic activity of the LAC@Co_xS_y-V/PMS system, the SMX degradation in different systems is carried out (Fig. 4), and the pseudo-first-order kinetics were also fitted (Table S5). As shown in Fig. 4a, PMS alone removed <5% of SMX, likely due to self-decomposition generating a small amount of ROS. LAC@Co_xS_y-V alone achieved ~10% removal through adsorption. In the LAC/PMS and Co_xS_y/PMS systems, SMX removal reached 29.61% and 26.91% within 30 min, respectively, which can be ascribed to weak PMS activation by LAC or Co_xS_y. Pre-adsorption tests confirmed <5% SMX uptake by LAC, excluding adsorption as the main factor. Thus, the modest removal in the LAC/PMS system is attributed to PMS activation via electron-donating C=O groups on LAC, highlighting its electron-transfer role and contribution to the synergistic performance of LAC@Co_xS_y-V.

While SMX degradation is rapidly increased to 94.57% in the LAC@Co_xS_y/PMS system with the relatively high mineralization efficiency of 29.63% (Fig. 4b). This significant improvement shows the synergistic catalytic activity of LAC@Co_xS_y towards PMS. This result is from the significant proportion of low-valence Co^{2+} species in LAC@Co_xS_y. A substantial number of Co^{3+} in Co_xS_y underwent reduction to Co^{2+} through the acceptance of electrons from the C=O groups of LAC. This accelerates the activation efficiency of PMS and yielded a substantial quantity of strong oxidizing $SO_4^{\bullet-}$. Consequently, the degradation and mineralization of SMX are enhanced. To verify this interpretation, the consumption kinetics of PMS were monitored as well (Fig. 4c). The rate of PMS decomposition in the LAC@Co_xS_y/PMS/SMX system is found to be 0.2127 min^{-1}, which is significantly higher than 0.0128 min^{-1} observed in the Co_xS_y/PMS/SMX system. Furthermore, SMX degradation performance in the LAC/Co_xS_y/PMS system (0.0521 min^{-1}) is weaker than LAC@Co_xS_y/PMS, thereby demonstrating the synergistic effect between LAC and Co_xS_y in PMS activation, rather than a simple physical superposition.

For the sulfur vacancies enriched LAC@Co_xS_y-V/PMS system (Fig. 4d), the K_{obs} of SMX degradation is 0.1517 min^{-1} with a mineralization of 53.71%, which shows nearly 2-fold enhancement in comparsion to the LAC@Co_xS_y/PMS system (0.0959 min^{-1} and 29.63%, respectively). This phenomenon can be attributed to the contribution of sulfur vacancies, which are produced during the grinding operation. The generation of vacancies increased the electronic density around the original Co atoms, thus causing the distribution of low-valence cobalt species and facilitating the PMS decomposition into $SO_4^{\bullet-}$. Conversely, the vacancies also promote the generation of $^1O_2$. The combined enhancement of $^1O_2$ and $SO_4^{\bullet-}$ leads to the promoted SMX degradation[34]. In contrast, the single PMS or LAC@Co_xS_y-V system only obtained 6.29% and 2.87% removal of SMX within 30 min, respectively. Concurrently, the contribution of the leaching amount of Co^{2+} on PMS activation was detected, and only 12.50% elimination of SMX is observed. This outcome is indicative of the exceptional efficacy of the LAC@Co_xS_y-V/PMS system.

As depicted in Fig. S2a, the effect of different concentrations of PMS on SMX removal was investigated. The single LAC@Co_xS_y-V system displays little influence on SMX removal, while with the PMS concentration increased from 0.1 mM to 0.4 mM, SMX could be degraded more than 95% within 30 min in each system, and the K_{obs} is enhanced from 0.0984 min^{-1} to 0.1771 min^{-1}, then reduced to 0.1650 min^{-1} with addition of PMS to 0.5 mM (Table S6 and Fig. S3). This indicates that reactive species were produced for SMX decomposition upon the addition of PMS in the reaction system. But as shown in Table S6, the growth rate of K_{obs} (ΔK_{obs}) is first increased, and then decreased with the increasing PMS concentration. The ΔK_{obs} reaches the maximum value when the concentration of PMS is 0.2 mM, as an excess amount of PMS may consume the produced ROS and the active sites of LAC@Co_xS_y-V are relatively insufficiet[35]. Therefore, 0.2 mM PMS was selected in a subsequent study.

In addition, the effect of LAC@Co_xS_y-V from 5 mg/L to 20 mg/L on SMX degradation was shown in Fig. S2b, and the pseudo-first-order kinetics were also fitted in Table S6 and Fig. S4. As with the study of PMS concentrations, a decrease in ΔK_{obs} is also observed under high LAC@Co_xS_y-V dosage, which could be attributed to relative supply of PMS. The competitive consumption of reactive species and excess catalysts result in diffusion restrictions in LAC@Co_xS_y-V/PMS/SMX system[36].According to Fig. S2c, the higher the LAC@Co_xS_y-V dosage is, the higher the cobalt ion dissolution. Considering the economic benefit and substrate removal efficiency, 10 mg/L catalyst was selected for further study.

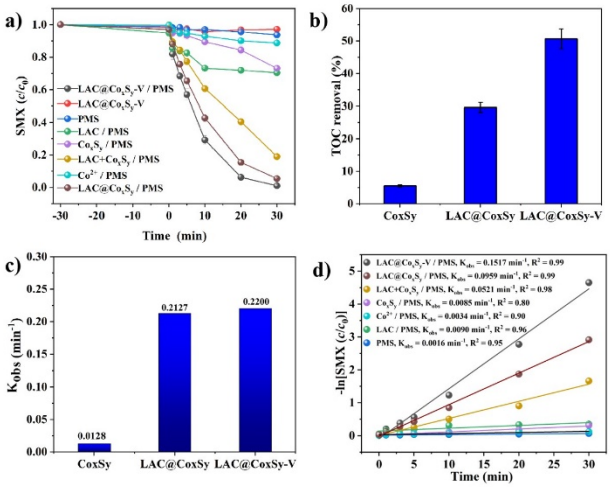

Fig. 4. (a) SMX degradation; (b) TOC removal; (c) The K_{obs} for PMS consumption; (d) Pseudo-first-order kinetic fitting curve in different systems. Conditions: $[SMX]_0$ = 5 mg/L; $[Catalyst]_0$ = 10 mg/L; $[PMS]_0$ = 0.2 mM, and pH = 5.1.

3.3 Mechanism for LAC@Co_xS_y-V activation of PMS

3.3.1 Identification of reactive species

The identification of various reactive and their contributions were identified by quenching experiments and EPR spectrums. Generally,

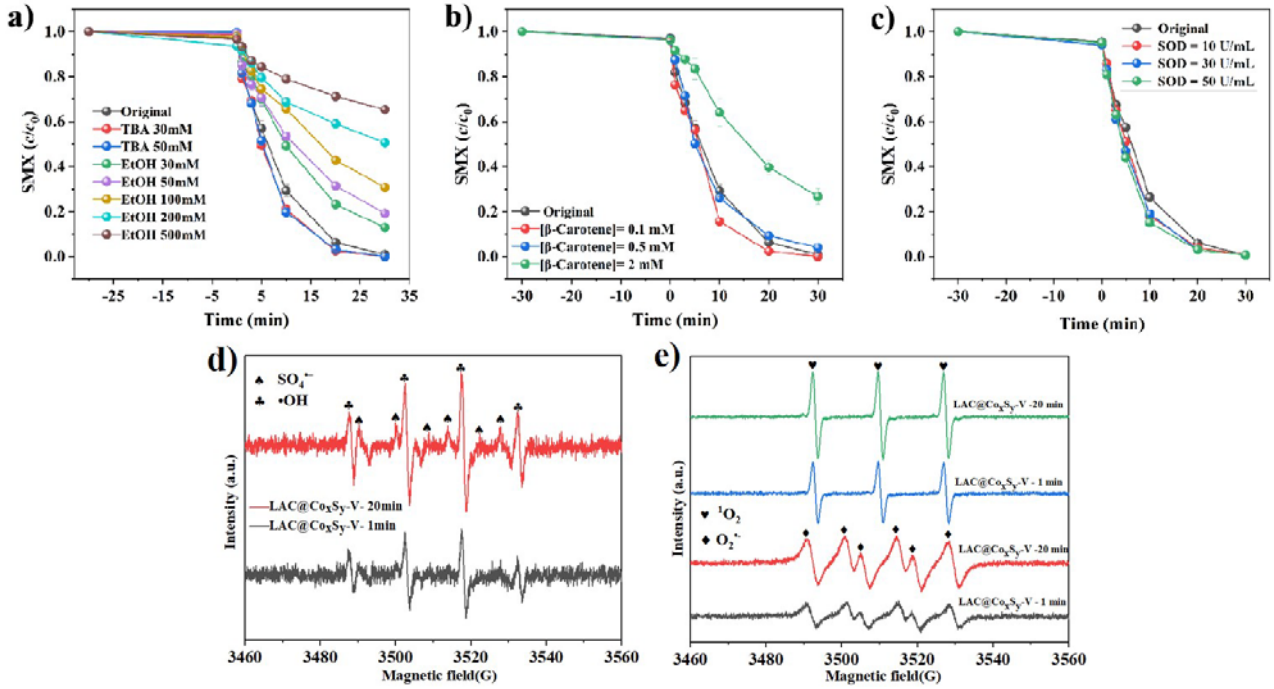

radical scavengers, i.e., EtOH and TBA were used to distinguish $SO_4^{\bullet-}$ and $^{\bullet}OH$, as EtOH with α-H readily reacts with both $SO_4^{\bullet-}$ (k_2 = 7.7×10^7 M^{-1}s^{-1}) and $^{\bullet}OH$ (k_2 = 2.8×10^9 M^{-1}s^{-1}))[9], while TBA without α-H reacts

Fig. 5. (a-c) Effect of different quenching agents on SMX degradation in the LAC@Co_xS_y-V/PMS system. (d-e) Identification of different ROS in the LAC@Co_xS_y-V/PMS system by EPR. Conditions: [SMX]$_0$ = 5 mg/L; [LAC@Co_xS_y-V]$_0$ = 10 mg/L; [PMS]$_0$ = 0.2 mM, and pH = 5.1.

with $^{\bullet}OH$ much faster than with $SO_4^{\bullet-}$ (k_2 = 4.0~9.1×10^5 M^{-1} s^{-1})[37]. β-carotene and superoxide dismutase (SOD) were selected as the scavengers of $^1O_2$ and $O_2^{\bullet-}$, respectively[38]. Methyl phenyl sulfoxide (PMSO) was employed to probe and quench high-valence cobalt (Co^{IV}=O^{2+}) (k_2 = 2.0 × 10^6 M^{-1} s^{-1}) [39].

As shown in Fig. 5a, 30-50 mM of TBA has no suppression on SMX degradation, results in slight enhancement. It might be due to the transformation of $^1O_2$ from the organic free radicals, which is generated through reactions between TBA and $^{\bullet}OH$[40]. And the degradation of SMX reduces from ~100% to 34.61%, with an excess of 500 mM EtOH. Meanwhile, a 26.68% decrease in SMX degradation is observed when the addition of β-carotene increased from 0.1 mM to 2 mM, indicating the participation of $^1O_2$ (Fig. 5b). In the case of 10-50 U/mL of SOD, little influence on SMX degradation is found (Fig. 5c), almost excluding the pathway for the generation of $^1O_2$ from $O_2^{\bullet-}$. In conclusion, $^{\bullet}OH$, $SO_4^{\bullet-}$, and $^1O_2$ all participates in the LAC@Co_xS_y-V/PMS system for SMX removal, where $SO_4^{\bullet-}$ is the main contributor

The existence of these ROS was further identified by EPR using DMPO and TEMP as the spin trappers. As depicted in Fig. 5d-e, the signals of $^{\bullet}OH$, $SO_4^{\bullet-}$, $^1O_2$ and $O_2^{\bullet-}$ are all observed in their specific spectrums. Since the contribution of $O_2^{\bullet-}$ on SMX removal is not obvious, it is speculated that the generation of $^1O_2$ via $O_2^{\bullet-}$ is limited. Furthermore, the signals are stronger as the reaction proceeding, indicating that the system can generate ROS all the time during PMS activation. Besides, the generation of $PMSO_2$ confirmed the presence of Co^{IV}=O^{2+} in Fig. S6 when employing PMSO into the catalysis system. However, its contribution to SMX degradation can be neglected, because the second-order rate constant of Co(IV) with SMX (k_2 = 1.6 × 10^7 M^{-1} s^{-1}) is almost two orders of magnitude lower than those of $SO_4^{\bullet-}$ (k_2 = 9.3 × 10^8 M^{-1} s^{-1}) [39, 41], and PMSO also competes with SMX for $SO_4^{\bullet-}$[42], further diminishing its apparent role. Therefore, although Co^{IV}=O^{2+} species are generated during PMS activation, the degradation of SMX is primarily governed by $SO_4^{\bullet-}$.

It has been determined that there are certain technical and theoretical disadvantages associated with quenching and EPR for determining ROS. In this study, various chemical probes were employed to evaluate the actual contribution of these ROS in the LAC@Co_xS_y-V/PMS system. Benzoic acid (BA) was used to analyze the occurrence of $^{\bullet}OH$ and $SO_4^{\bullet-}$ ($k_{(\bullet OH,\ BA)}$= 3.9 × 10^9 M^{-1} s^{-1}, $k_{(SO4\bullet-,\ BA)}$ = 1.2 × 10^9 M^{-1} s^{-1}). Nitrobenzene (NB) was widely used to identify •OH ($k_{(\bullet OH,\ NB)}$= 5.9 × 10^9 M^{-1}s^{-1}) [43]. Metronidazole (MDZ) has been frequently regarded as an effective detector for the quantification of $^1O_2$ and $^{\bullet}OH$ ($k_{(\bullet OH)}$= 6 × 10^9 M^{-1} s^{-1}, $k_{(1O2)}$ = 1.5 × 10^8 M^{-1} s^{-1})[43]. The precise calculations can be found in Text S3. Results shows that the contribution of $^{\bullet}OH$, $SO_4^{\bullet-}$ and $^1O_2$ occupied ~4%, 74%, and 22%, respectively. This conclusion is consistent with the quenching experiments. This may also corroborate our initial hypothesis that the amalgamation of strategies, namely the acceptance of electrons from the C=O groups of LAC and the generation of vacancies through grinding, can facilitate the synthesis of low-valence cobalt species. This, in turn, has the potential to enhance the PMS activation process, thereby augmenting $SO_4^{\bullet-}$ production.

3.3.2 Mechanism of the generation of ROS.

Based on quenching experiments, EPR monitoring, and calculation of molecular probe compounds, it has been verified that $SO_4^{\bullet-}$ plays a dominant role, while $^1O_2$ also contributes to some extent. The following is a proposed pathway for the generation of ROS in the LAC@Co_xS_y-V/PMS system. In the study of $SO_4^{\bullet-}$, an analysis was conducted of the XPS fitting of Co 2p and S 2p spectra of LAC@Co_xS_y-V before and after the reaction (Fig. 6a-b). This indicates the presence of Co^{3+} on the surface of LAC@Co_xS_y-V after the reaction, as well as an increase in the relative content of S_2^{2-}. Thus, it is hypothesized that Co^{2+} would activate HSO_5^- to generate $SO_4^{\bullet-}$ and Co^{3+} (Eq. 1). Co^{3+} can be reduced back to Co^{2+} via the following pathways: a) by HSO_5^-, b) by using S^{2-} as an electron donor (Eq. 2-4)[44], and c) by capturing a vacancy delocalized electron for reduction (Eq. 5)[45]. The enriched existence of original Co^{2+} and the new-reduced Co^{2+} ensures uninterrupted production of $SO_4^{\bullet-}$ by the redox cycle of Co^{3+}/Co^{2+}. $^{\bullet}OH$ formation can result from the activation of PMS by Co^{2+} (as Eq. 6), or the hydrolysis of $SO_4^{\bullet-}$ (as Eq. 7).

In terms of $^1O_2$, the pathway of its generation is speculated as follows: a) the vacancies adsorbs the dissolved oxygen to produce $^1O_2$ via $O_2^{\bullet-}$ (Eq.8-9)[46], as the K_{obs} of 0.1129 min^{-1} for SMX degradation under N_2 atmosphere is slightly lower than that under air atmosphere (0.1372 min^{-1}) (Fig. 6c); b) sulfur vacancies can also obtain electrons from PMS to produce $SO_5^{\bullet-}$, thereby produces $^1O_2$ (Eq.10); c) the exsiting $^{\bullet}OH$ could also converted into $^1O_2$ via dismutation reactions (Eq.11)[6].

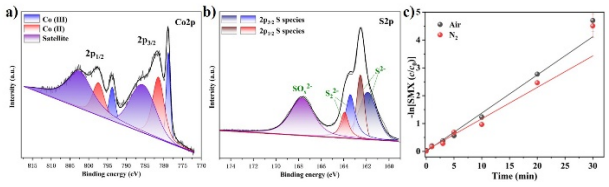

Fig. 6. (a) Co 2p and (b) S 2p spectra of the used LAC@Co_xS_y-V. (c) Pseudo-first-order kinetic fitting curves of SMX degradation under air and N_2 in the LAC@Co_xS_y-V/PMS system. Conditions: $[SMX]_0$ = 5 mg/L; $[LAC@Co_xS_y\text{-}V]_0$ = 10 mg/L; $[PMS]_0$ = 0.2 mM, and pH = 5.1.

$$Co^{2+} + HSO_5^- \rightarrow Co^{3+} + SO_4^{\cdot-} + OH^- \quad (1)$$

$$Co^{3+} + HSO_5^- \rightarrow Co^{2+} + SO_5^{\cdot-} + H^+ \quad (2)$$

$$S^{2-} \rightarrow S_2^{2-} + Sn^{2-} + e^- \quad (3)$$

$$Co^{3+} + e^- \rightarrow Co^{2+} \quad (4)$$

$$Co^{3+} + e^-(SVs) \rightarrow Co^{2+} \quad (5)$$

$$Co^{2+} + HSO_5^- \rightarrow Co^{3+} + \cdot OH + SO_4^{2-} \quad (6)$$

$$SO_4^{\cdot-} + H_2O \rightarrow \cdot OH + SO_4^{2-} + H^+ \quad (7)$$

$$O_2 + e^-(SVs) \rightarrow O_2^{\cdot-} \quad (8)$$

$$O_2^{\cdot-} + 2H_2O \rightarrow {}^1O_2 + H_2O_2 + 2OH^- \quad (9)$$

$$HSO_5^-(SVs) \rightarrow SO_5^{\cdot-} \rightarrow {}^1O_2 \quad (10)$$

$$4\cdot OH \rightarrow {}^1O_2 + 2H_2O \quad (11)$$

To further determine the role of the C=O group in the production of low-valence cobalt ions in PMS activation, the formation of ROS in the Co_xS_y/PMS was also identified through EPR and quenching experiments. For the Co_xS_y/PMS system, the EPR results (Fig. 7a-b) shows that there are $^{\bullet}OH$, $SO_4^{\bullet-}$, and $^1O_2$. Ethanol is capable of scavenging both $SO_4^{\bullet-}$ and $^{\bullet}OH$ reactive species [9]. In contrast, the Co_xS_y system displayed much weaker and broader EPR signals for $O_2^{\bullet-}$ compared to LAC@CoxSy-V, suggesting a lower efficiency in $O_2^{\bullet-}$ generation. However, the degradation of SMX is not significantly inhibited after the addition of 30 mM~100 mM EtOH (as Fig. 7c), indicating that $^{\bullet}OH$ and $SO_4^{\bullet-}$ are not the main ROS, while $^1O_2$ is the main contributors to SMX degradation.

For the LAC@Co_xS_y/PMS system (Fig. 7d), adding 50-200 mM EtOH leads to a maximum of 64% inhibition on SMX degradation within 30 min, while the addition of TBA has no inhibitory effect. It suggests that $SO_4^{\bullet-}$ plays a major role in SMX degradation. Thus, it could be concluded that the main ROS varied from $^1O_2$ (or other non-radical pathways) to $SO_4^{\bullet-}$ after the cobalt sulfides catalyst combining with LAC. This phenomenon could be ascribed to the reduction of massive Co^{3+} into Co^{2+} by the surface C=O groups of LAC, enhancing the yield of $SO_4^{\bullet-}$ by PMS activation. For the LAC@Co_xS_y-V/PMS system, the presence of abundant sulfur vacancies further provides more low-coordinated cobalt sites for activating PMS to generate $SO_4^{\bullet-}$. Meanwhile, $^{\bullet}OH$ may be generated through the hydrolysis of $SO_4^{\bullet-}$ or the reaction between Co^{2+} and HSO_5^- (Eqs. 6-7).

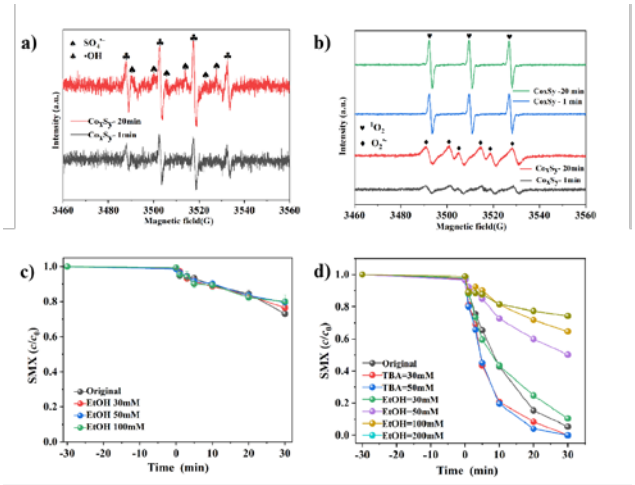

Fig. 7. (a, b) EPR spectra of ROS in the Co_xS_y/PMS system; (c) SMX degradation efficiency in the presence of EtOH in the Co_xS_y/PMS system; (d) SMX degradation efficiency in the LAC@Co_xS_y/PMS system with addition of TBA or EtOH. Conditions: $[SMX]_0$ = 5 mg/L; $[Co_xS_y$ or LAC@$Co_xS_y]_0$ = 10 mg/L; $[PMS]_0$ = 0.2 mM, and pH = 5.1.

3.4 The possible degradation pathways of SMX.

In order to investigate the transformation pathway of SMX, LC-MS was utilized to analyze the degradation intermediates. A total of 13 intermediates of SMX from the LAC@Co_xS_y-V/PMS system was identified and the detection of key MS fragments was provided in Table S7. There are three possible degradation pathways according to the detected molecules, as described in Fig. 8. Among them, pathway (a) is considered the

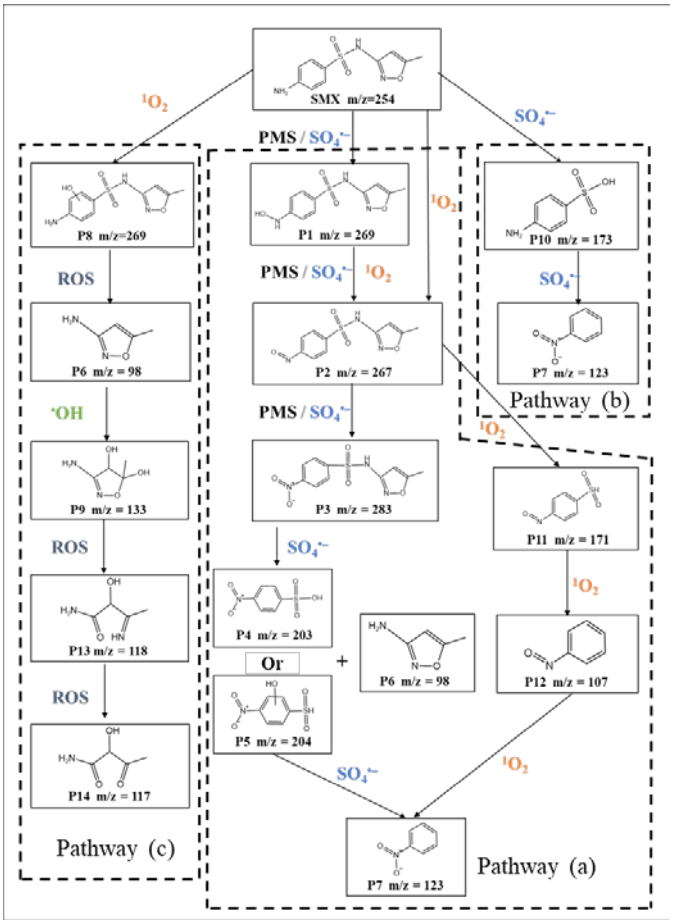

Fig. 8. Proposed reactive oxygen species-mediated degradation pathways of SMX in the LAC@Co_xS_y-V/PMS system, as elucidated by LC-MS.

dominant route, consistent with the quenching and probe results showing $SO_4^{\bullet-}$ as the major ROS. It involves the reaction of $SO_4^{\bullet-}$ with phenol, aniline, and olefin of organics through radical adduct formation, hydrogen atom abstraction and single electron transfer pathways, thereby generating free radicals centered on N atoms of the amine group, then aniline radical. Subsequent to this initial reaction, the substance undergoes a secondary reaction with oxygen, resulting in the formation of hydroxylamine (P1) and nitroso derivatives (P2). These derivatives, in turn, encounter a hydrolysis process, yielding nitrosulfa metharomodolzol (P3). Although HSO_5^- could oxidize aniline into nitrate (SMX→P1→P2→P3) at the initial step, the N-S or C-S bonds of SMX are difficult to be cracked into small fractions due to its limited oxidizing activity. While P3 could be oxidized into P4 (or P5) and P6 by $SO_4^{\bullet-}$[47], and the further oxidation product (P7) is detected. As shown pathway (b), sulfonation through radical addition is the characteristic pathway of $SO_4^{\bullet-}$, which is confirmed by the detection of P10[48].

In the context of pathway (c), $^1O_2$, a highly selective oxidant, reacts almost exclusively with unsaturated organics via electrophilic addition and electron abstraction. Apart from pathway (a), the detection of nitro-compound P2 via the oxidation of amino group of P1 indicates the participation of $^1O_2$ oxidation. Then, the N-S bond is cleaved and forms into P11 by the attack of $^1O_2$[48]. Additionally, P8 could be the additive product of SMX and $^1O_2$, leading to the formation of P6. P9 and P13 are the further oxidation products of P8 through the substitution of •OH[34].

Overall, these results illustrate that SMX degradation proceeds primarily through $SO_4^{\bullet-}$-driven radical pathways, with supplementary contributions from $^1O_2$ and minor •OH. Ultimately, these intermediates can proceed to further degradation, yielding smaller organic molecules, H_2O, and CO_2.

3.5 Practical application of LAC@Co_xS_y-V/PMS system

3.5.1 Influence of co-existing inorganic anions and natural organic matters

To explore the practical application potential of the LAC@Co_xS_y-V/PMS system, the effects of various background substances (Cl^-, $H_2PO_4^-$, HPO_4^{2-}, SO_4^{2-}, HCO_3^-, HA, etc.) on SMX removal were investigated (Fig. S5). The presence of Cl^-, $H_2PO_4^-$, and HPO_4^{2-} enhances SMX removal in a concentration-dependent manner, with the promotion being more pronounced at higher concentrations. Cl^- could react with $SO_4^{\bullet-}$ to generate oxidative chloride radicals, including $Cl^\bullet$ and $Cl_2^{\bullet-}$[49]. Additionally, an excess of Cl^- can react with PMS to generate HClO or ClO^- with strong oxidizing ability[50]. $H_2PO_4^-$ and HPO_4^{2-} may reduce bond dissociation energy by interacting with PMS and pollutants or by forming complexes with Co^{2+} sites on the LAC@Co_xS_y-V surface[51]. The slight improvement in SMX degradation observed with low concentrations of HCO_3^- can be attributed to pH changes induced by its addition[52]. Although high concentration of SO_4^{2-} shows a minor inhibitory effect on SMX removal at the initial stage of the reaction (Fig. S5d-e), complete degradation is still achieved within 30 min. The presence of HA from 1 to 10 mg/L inhibits SMX degradation in the LAC@Co_xS_y-V/PMS system (Fig. S5f), which may be due to the adsorption of HA onto the LAC@Co_xS_y-V surface, blocking active sites, thereby suppressing ROS generation and reducing degradation efficiency[53, 54]. Overall, the coexistence of inorganic anions and HA generally exerts limited adverse effects on SMX removal, and the LAC@Co_xS_y-V/PMS system demonstrates considerable potential in real wastewater.

3.5.2 Stability and reusability of LAC@CoxSy-V

The cycling stability is important for evaluating its suitability for practical applications. Herein, the cyclic degradation of SMX was executed by continuously adding PMS (Fig. 9a). Nearly total SMX degradation within 30 min is achieved in each entry after 5-round operations, indicating the excellent recyclability of LAC@Co_xS_y-V. Meanwhile, the concentration of leached Co^{2+} was detected to be 0.2-0.4 mg/L (Fig. 9b). Therefore, the LAC@Co_xS_y-V/PMS is sufficiently stable with high efficiency towards SMX removal. In addition, post-reaction XRD spectra of LAC@Co_xS_y-V also shows that the characteristic diffraction peaks of LAC@Co_xS_y-V are almost retained, and no new oxide reflections observed (Fig. S7). This further confirms that the LAC@Co_xS_y-V structure persists after a long-term reaction.

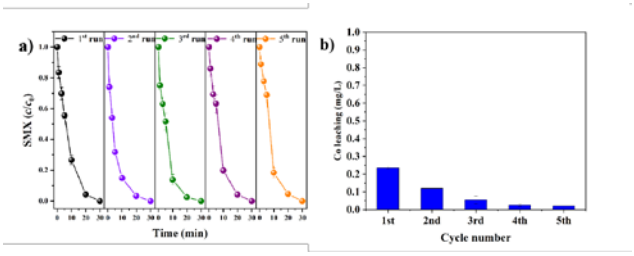

Fig. 9. (a) Recyclability and stability of LAC@Co_xS_y-V/PMS system, (b) The leaching of cobalt ions after each run. Conditions: $[SMX]_0$ = 5 mg/L; $[LAC@Co_xS_y\text{-}V]_0$ = 10 mg/L; $[PMS]_0$ = 0.2 mM, and pH = 5.1

3.5.3 COD removal efficiency of the simulated wastewater treatment system

Following the investigation of the effects of inorganic anions, and HA on SMX degradation in the LAC@Co_xS_y-V/PMS system. This investigation was complemented by an assessment of the cyclic stability of LAC@Co_xS_y-V. Then, the COD removal efficiency for simulated medical wastewater was demonstrated using a continuous-flow fixed-bed reactor (details of the simulated wastewater are provided in Table S8). This study aims to further assess the potential of the LAC@Co_xS_y-V/PMS system for treating actual medical wastewater. The wastewater treatment system (the schematic diagram shown in the Fig. 10a) mainly incorporated with a mixing reservoir of PMS and simulated wastewater, a peristaltic pump, and a continuous flow fixed bed reactor (with a packed bed loaded with LAC@Co_xS_y-V). In the packed bed, a total of 12 melamine sponges loaded with LAC@Co_xS_y-V were installed, with a loading of approximately 3.82 mg/cm^3. The influent flow rate was maintained at 10 mL/min. As shown in Fig. 10b, continuous monitoring of COD removal efficiency over a 10-hour period revealed that over 70% of COD was removed within the first 4 hours. The COD removal rate in the first hour is slightly lower than that in the subsequent 2 hours, likely due to the dry state of the LAC@Co_xS_y-V carrier sponges at the beginning of the operation. It hinders the flow of wastewater through the sponge, resulting in a stronger edge effect. Besides, the COD removal efficiency gradually decreased from the 5th hour, which can be attributed to the gradual reduction of active sites of LAC@Co_xS_y-V during the continuous reaction process. Overall, the system demonstrates relatively high COD removal performance over the 10-hour continuous operation, further highlighting the potential of the LAC@Co_xS_y-V/PMS system for practical medical wastewater treatment applications.

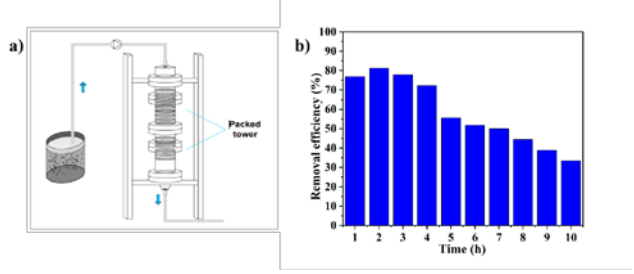

Fig. 10. (a) Schematic diagram of a simulated wastewater treatment system; (b) COD removal efficiency of simulated wastewater in the LAC@Co_xS_y-V/PMS system.

4. Conclusion

In summary, the LAC supported cobalt sulfide with enriched sulfur vacancies (LAC@Co_xS_y-V) was successfully synthesized, and the performance and mechanism of the LAC@Co_xS_y-V/PMS system for sulfamethoxazole (SMX) degradation were systematically elucidated. The LAC@Co_xS_y-V/PMS system achieved approaching complete sulfamethoxazole (SMX) removal efficiency within 30 mins, which is three times higher than the unmodified Co_xS_y/PMS system. Through XPS analysis, EPR spectroscopy, quenching experiments, and chemical probes, it was discovered that $SO_4^{\bullet-}$ was the primary contributor to SMX removal. Specifically, $SO_4^{\bullet-}$ was generated primarily through the activation of PMS by the low-valence cobalt species, which were abundant due to electron transfer from the electronegative oxygen in the carbonyl groups on the LAC surface to Co^{3+}, as well as the further enhancement of Co^{2+} proportions by sulfur vacancies. Conversely, $^1O_2$ was primarily produced through the conversion of adsorbed oxygen from the air and dissolved oxygen facilitated by the sulfur vacancies. Additional experiments were conducted to investigate the effects of inorganic anions (Cl^-, $H_2PO_4^-$, and HPO_4^{2-}, etc.), and humic acid (HA) on SMX degradation, which confirmed the robust interference resistance and wide applicability of this system. Cyclic stability tests revealed that the LAC@Co_xS_y-V/PMS system could achieve stable and efficient recycling for more than 5 cycles. Furthermore, a simulated medical wastewater COD removal experiment relatively high COD removal performance over the 10-hour continuous operation, demonstrating the potential of the system for medical wastewater treatment. Overall, this work offered a novel and feasible strategy for enhancing the efficiency of cobalt sulfide catalysts in activating PMS and constructing sulfate radical-based advanced oxidation processes (SR-AOPs) for the treatment of medical wastewater.

Author contributions

Liyuan Wu: Conceptualization, Writing – review & editing, Project administration, Methodology, Supervision, Funding acquisition. **Chaoyang Wang**: Writing, Data curation, Software, Validation, Methodology. **Xin Wang**: Writing, Data curation, Formal Analysis. **Xun Zhang**: Methodology, Investigation. **Qian Yu**: Investigation, Resources. **Yuanyuan Jiang**: Data curation, Visualization. **Kaiyu Chen**: Software, Validation. **Wenli Yang**: Visualization, Writing – review & editing. **Pengpeng Guo**: Supervision, Writing – review & editing. **Haiyan Li**: Resources, Project administration.

Conflicts of interest

The authors declare that they have no known competing financial interests or personal relationships that could have appeared to influence the work reported in this paper.

Acknowledgments

This work was supported by the National Natural Science Foundation of China (No. 52100001 and 51978032); the Youth Beijing Scholars program (No. 024).

References

1. F. Liu, H. Zhou, Z. Pan, Y. Liu, G. Yao, Y. Guo and B. Lai, Degradation of sulfamethoxazole by cobalt-nickel powder composite catalyst coupled with peroxymonosulfate: Performance, degradation pathways and mechanistic consideration, *J Hazard Mater*, 2020, **400**, 123322.
2. T. B. Minh, H. W. Leung, I. H. Loi, W. H. Chan, M. K. So, J. Q. Mao, D. Choi, J. C. W. Lam, G. Zheng, M. Martin, J. H. W. Lee, P. K. S. Lam and B. J. Richardson, Antibiotics in the Hong Kong metropolitan area: Ubiquitous distribution and fate in Victoria Harbour, *Marine Pollution Bulletin*, 2009, **58**, 1052-1062.
3. Z. Meng, C. Li, G. Zhao, Y. Yang, Y. Yan, C. Hu and W. J. J. o. E. C. E. Wang, Activation mechanism of persulfate by acidified oil shale semi-coke for catalytic degradation of volatile phenols: the synergistic effect of transition metal and surface organic matter, 2025, 115780.
4. Z.-B. Lv, L. Xu, C. Chen, Z.-H. Chen, M.-L. Fu and B. J. J. o. E. C. E. Yuan, Selective recovery of lithium from spent LiFePO4 batteries based on PMS advanced oxidation process, 2025, 115735.
5. L. Mengmeng, Z. Jing, L. Yuheng, G. Feilong, L. Rui, C. Hong, Z. Meng, J. Qike, L. Jian and Y. Sheng, Modulating the electronic structures of layer-expanded MoS2 nanoreactor via cobalt doping and carbon intercalation for enhanced electrocatalytic hydrogen evolution %J Chemical Engineering Journal, 2022, **446**.
6. H. Zeng, L. Deng, H. Zhang, C. Zhou and Z. Shi, Development of oxygen vacancies enriched CoAl hydroxide@hydroxysulfide hollow flowers for peroxymonosulfate activation: A highly efficient singlet oxygen-dominated oxidation process for sulfamethoxazole degradation, *J Hazard Mater*, 2020, **400**, 123297.
7. L. Wu, P. Guo, X. Wang, H. Li, A. Li and K. Chen, Mechanism study of CoS2/Fe(III)/peroxymonosulfate catalysis system: The vital role of sulfur vacancies, *Chemosphere*, 2022, **288**, 132646.
8. Y. Li, W. Zhu, Q. Guo, X. Wang, L. Zhang, X. Gao and Y. Luo, Highly efficient degradation of sulfamethoxazole (SMX) by activating peroxymonosulfate (PMS) with CoFe2O4 in a wide pH range, *Separation and Purification Technology*, 2021, **276**.
9. L. Gao, Y. Guo, J. Zhan, G. Yu and Y. Wang, Assessment of the validity of the quenching method for evaluating the role of reactive species in pollutant abatement during the persulfate-based process, *Water Res*, 2022, **221**, 118730.
10. L. Wu, Z. Sun, Y. Zhen, S. Zhu, C. Yang, J. Lu, Y. Tian, D. Zhong and J. Ma, Oxygen Vacancy-Induced Nonradical Degradation of Organics: Critical Trigger of Oxygen (O2) in the Fe–Co LDH/Peroxymonosulfate System, *Environmental Science & Technology*, 2021, **55**, 15400-15411.
11. W. Liyuan, G. Pengpeng, W. Xin, L. Haiyan, Z. Xiaoran, C. Kaiyu and Z. Peng, The synergy of sulfur vacancies and heterostructure on CoS@FeS nanosheets for boosting the peroxymonosulfate activation, *Chem. Eng. J.*, 2022, **446**.
12. M. L. C. dos Reis, T. d. J. Santos, L. A. de Albuquerque, C. S. Felix, L. S. Teixeira and F. d. S. J. M. J. Dias, Comparison of green analytical procedures based on activated persulfate reactions for organic chemical degradation for multi-element determination in honey samples by ICP OES, 2025, **210**, 112926.
13. Y. Li, C. Li, K. Zhang and J. J. C. L. Cao, Degradation of Tetracyclines in Water by Activating Peroxymonosulfate with Zeolitic Imidazolate Framework 67 Derivatives, 2025, **155**, 94.
14. G. Blyholder, Molecular Orbital View of Chemisorbed Carbon Monoxide, *The Journal of Physical Chemistry*, 1964, **68**, 2772-2777.
15. M. J. Drance, J. D. Sears, A. M. Mrse, C. E. Moore, A. L. Rheingold, M. L. Neidig and J. S. Figueroa, Terminal coordination of diatomic boron monofluoride to iron, 2019, **363**, 1203-1205.
16. W. Unkrig, M. Schmitt, D. Kratzert, D. Himmel and I. Krossing, Synthesis and characterization of crystalline niobium and tantalum carbonyl complexes at room temperature 成键, *Nature chemistry*, 2020, **12**, 647-653.
17. Y. Haixian, P. Yusong, L. Xiaobo, Z. Yuan, H. Run and P. Chengling, Metal organic framework derived CuSx/C with plentiful S-vacancies for efficient heterogenous activation of peroxymonosulfate, *Appl. Surf. Sci.*, 2023, **607**.
18. Z. Li, S. Ma, L. Sang, G. Qu, T. Zhang, B. Xu, W. Jin and Y. Zhao, Enhanced arsenite removal from water using zirconium-ferrocene MOFs coupled with peroxymonosulfate:oxidation and multi-sites

adsorption mechanism, *Chemosphere*, 2023, **319**, 138044.

19. L. Jing, M. Xie, Y. Xu, C. Tong, X. Du, H. Zhao, N. Zhong, H. Li and J. Hu, Advanced oxidation via the synergy of C-defective/C-O band modified ultrathin porous g-C_3N_4 and PMS for efficient photothermal degradation of bisphenol pollutants and lignin derivatives %J Green Energy & Environment, 2024, **9**, 1159-1170.
20. Y. Zhang, C. Li, Y. Zhu, X. Du, Y. Lyu, S. Li and Y. Zhai, Insight into the enhanced performance of toluene removal from simulated flue gas over Mn-Cu oxides modified activated coke, *Fuel*, 2020, **276**.
21. W. Ma, S. Zhang, Y. Chen, D. Zhong, Q. Du, J. Li, R. Li, X. Du, J. Zhang and T. Yu, Fe3O4-CuO@Lignite activated coke activated persulfate advanced treatment of phenolic wastewater from coal chemical industry, *Environ Res*, 2022, DOI: 10.1016/j.envres.2022.113601, 113601.
22. E. Marín, X. Vendrell and J. J. A. A. N. M. Llorca, Pd Supported on CeO2 Nanostructures Prepared by Planetary Ball Milling under a Modified Atmosphere for Catalytic Oxidation of CO, 2025.
23. Q. Ma, L.-c. Nengzi, B. Li, Z. Wang, L. Liu and X. Cheng, Heterogeneously catalyzed persulfate with activated carbon coated with CoFe layered double hydroxide (AC@CoFe-LDH) for the degradation of lomefloxacin, *Separation and Purification Technology*, 2020, **235**.
24. Y. Li, K. Yin, L. Wang, X. Lu, Y. Zhang, Y. Liu, D. Yan, Y. Song and S. Luo, Engineering MoS2 nanomesh with holes and lattice defects for highly active hydrogen evolution reaction, *Applied Catalysis B: Environmental*, 2018, **239**, 537-544.
25. L. Wu, C. Du, J. He, Z. Yang and H. Li, Effective adsorption of diclofenac sodium from neutral aqueous solution by low-cost lignite activated cokes, *J Hazard Mater*, 2020, **384**, 121284.
26. S. Jia, J. Wei, B. Gong, J. Wei and Z. Shao, Sulfur vacancies enriched Nickel-Cobalt sulfides hollow spheres with high performance for All-Solid-State hybrid supercapacitor, *Journal of Colloid and Interface Science*, 2021, **601**, 640-649.
27. L. Kang, C. Huang, J. Zhang, M. Zhang, N. Zhang, S. Liu, Y. Ye, C. Luo, Z. Gong, C. Wang, X. Zhou, X. Wu and S. C. Jun, Effect of fluorine doping and sulfur vacancies of CuCo2S4 on its electrochemical performance in supercapacitors, *Chemical Engineering Journal*, 2020, **390**, 124643.
28. F. Sun, C. Yang, Z. Qu, W. Zhou, Y. Ding, J. Gao, G. Zhao, D. Xing and Y. Lu, Inexpensive activated coke electrocatalyst for high-efficiency hydrogen peroxide production: Coupling effects of amorphous carbon cluster and oxygen dopant, *Applied Catalysis B: Environmental*, 2021, **286**.
29. L. Long, X. Liu, L. Chen, S. Wang, M. Liu and J. Jia, MOF-derived 3D leaf-like CuCo oxide arrays as an efficient catalyst for highly sensitive glucose detection, *Electrochimica Acta*, 2019, **308**, 243-252.
30. L. Jing, M. Xie, Y. Xu, C. Tong, X. Du, H. Zhao, N. Zhong, H. Li and J. Hu, Advanced oxidation via the synergy of C-defective/ C–O band modified ultrathin porous g-C3N4 and PMS for efficient photothermal degradation of bisphenol pollutants and lignin derivatives, *Green Energy & Environment*, 2023, DOI: https://doi.org/10.1016/j.gee.2023.01.006.
31. H. Qian, J. Tang, Z. Wang, J. Kim, J. H. Kim, S. M. Alshehri, E. Yanmaz, X. Wang and Y. Yamauchi, Synthesis of Cobalt Sulfide/Sulfur Doped Carbon Nanocomposites with Efficient Catalytic Activity in the Oxygen Evolution Reaction, *Chemistry*, 2016, **22**, 18259-18264.
32. Y. Huang, W. Zhou, L. Xie, J. Li, Y. He, S. Chen, X. Meng, J. Gao and Y. Qin, Edge and defect sites in porous activated coke enable highly efficient carbon-assisted water electrolysis for energy-saving hydrogen production, *Renewable Energy*, 2022, **195**, 283-292.
33. L. Amirache, F. Barka-Bouaifel, P. Borthakur, M. R. Das, H. Ahouari, H. Vezin, A. Barras, B. Ouddane, S. Szunerits and R. Boukherroub, Cobalt sulfide-reduced graphene oxide: An efficient catalyst for the degradation of rhodamine B and pentachlorophenol using peroxymonosulfate, *Journal of Environmental Chemical Engineering*, 2021, **9**.
34. L. Wu, P. Guo, X. Wang, H. Li, X. Zhang, K. Chen and P. Zhou, The synergy of sulfur vacancies and heterostructure on CoS@FeS nanosheets for boosting the peroxymonosulfate activation, *Chemical Engineering Journal*, 2022, **446**, 136759.
35. Q. Ye, J. Wu, P. Wu, J. Wang, W. Niu, S. Yang, M. Chen, S. Rehman and N. Zhu, Enhancing peroxymonosulfate activation of Fe-Al layered double hydroxide by dissolved organic matter:

Performance and mechanism, *Water Research*, 2020, **185**, 116246.
36. T. Zhang, H. Zhu and J.-P. Croué, Production of Sulfate Radical from Peroxymonosulfate Induced by a Magnetically Separable CuFe2O4 Spinel in Water: Efficiency, Stability, and Mechanism, *Environmental Science & Technology*, 2013, **47**, 2784-2791.
37. Y.-Y. Ahn, J. Choi, M. Kim, M. S. Kim, D. Lee, W. H. Bang, E.-T. Yun, H. Lee, J.-H. Lee, C. Lee, S. K. Maeng, S. Hong and J. Lee, Chloride-Mediated Enhancement in Heat-Induced Activation of Peroxymonosulfate: New Reaction Pathways for Oxidizing Radical Production, *Environmental Science & Technology*, 2021, **55**, 5382-5392.
38. X. Xie, J. Cao, Y. Xiang, R. Xie, Z. Suo, Z. Ao, X. Yang and H. Huang, Accelerated iron cycle inducing molecular oxygen activation for deep oxidation of aromatic VOCs in MoS2 co-catalytic Fe3+/PMS system, *Applied Catalysis B: Environmental*, 2022, **309**.
39. Y. Zong, X. Guan, J. Xu, Y. Feng, Y. Mao, L. Xu, H. Chu and D. Wu, Unraveling the Overlooked Involvement of High-Valent Cobalt-Oxo Species Generated from the Cobalt(II)-Activated Peroxymonosulfate Process, *Environ Sci Technol*, 2020, **54**, 16231-16239.
40. L. Wang, B. Li, D. D. Dionysiou, B. Chen, J. Yang and J. Li, Overlooked Formation of H2O2 during the Hydroxyl Radical-Scavenging Process When Using Alcohols as Scavengers, *Environmental Science & Technology*, 2022, **56**, 3386-3396.
41. J. Liang, X. Duan, X. Xu, K. Chen, Y. Zhang, L. Zhao, H. Qiu, S. Wang and X. Cao, Persulfate Oxidation of Sulfamethoxazole by Magnetic Iron-Char Composites via Nonradical Pathways: Fe(IV) Versus Surface-Mediated Electron Transfer, *Environmental Science & Technology*, 2021, **55**, 10077-10086.
42. Z. Wang, W. Qiu, S. Pang, Y. Gao, Y. Zhou, Y. Cao and J. Jiang, Relative contribution of ferryl ion species (Fe(IV)) and sulfate radical formed in nanoscale zero valent iron activated peroxydisulfate and peroxymonosulfate processes, *Water Research*, 2020, **172**, 115504.
43. X. Liu, Y. Hong, S. Ding, W. Jin, S. Dong, R. Xiao and W. Chu, Transformation of antiviral ribavirin during ozone/PMS intensified disinfection amid COVID-19 pandemic, *Science of The Total Environment*, 2021, **790**, 148030.
44. Y. Ding, Y. Hu, X. Peng, Y. Xiao and J. Huang, Micro-nano structured CoS: An efficient catalyst for peroxymonosulfate activation for removal of bisphenol A, *Separation and Purification Technology*, 2020, **233**, 116022.
45. J. Lim, Y. Yang and M. R. Hoffmann, Activation of Peroxymonosulfate by Oxygen Vacancies-Enriched Cobalt-Doped Black TiO2 Nanotubes for the Removal of Organic Pollutants, *Environmental Science & Technology*, 2019, **53**, 6972-6980.
46. Q. Yi, J. Ji, B. Shen, C. Dong, J. Liu, J. Zhang and M. Xing, Singlet Oxygen Triggered by Superoxide Radicals in a Molybdenum Cocatalytic Fenton Reaction with Enhanced REDOX Activity in the Environment, *Environ Sci Technol*, 2019, **53**, 9725-9733.
47. C. Ling, X. Liu, M. Li, X. Wang, Y. Shi, J. Qi, J. Zhao and L. Zhang, Sulphur vacancy derived anaerobic hydroxyl radical generation at the pyrite-water interface: Pollutants removal and pyrite self-oxidation behavior, *Applied Catalysis B: Environmental*, 2021, **290**, 120051.
48. D. T. Oyekunle, E. A. Gendy, J. Ifthikar and Z. Chen, Heterogeneous activation of persulfate by metal and non-metal catalyst for the degradation of sulfamethoxazole: A review, *Chemical Engineering Journal*, 2022, **437**.
49. H. Luo, Y. Cheng, Y. Zeng, K. Luo, D. He and X. Pan, Rapid removal of organic micropollutants by heterogeneous peroxymonosulfate catalysis over a wide pH range: Performance, mechanism and economic analysis, *Separation and Purification Technology*, 2020, **248**, 117023.
50. B. Shao, C. Hu, H. Zhao, C. Xiao, E. Du, A. Cai and J. Deng, Degradation of ambroxol by UV/chloramine process: Kinetics, degradation pathway, and control of the risk of highly toxic disinfection by-products, *Environ Pollut*, 2024, **363**, 125091.
51. N. Li, Y. Wang, X. Cheng, H. Dai, B. Yan, G. Chen, L. a. Hou and S. Wang, Influences and mechanisms of phosphate ions onto persulfate activation and organic degradation in water treatment: A review, *Water Research*, 2022, **222**, 118896.
52. J. Wang and S. Wang, Reactive species in advanced oxidation processes: Formation, identification and reaction mechanism, *Chemical Engineering Journal*, 2020, **401**, 126158.

53. C. Gong, F. Chen, Q. Yang, K. Luo, F. Yao, S. Wang, X. Wang, J. Wu, X. Li, D. Wang and G. Zeng, Heterogeneous activation of peroxymonosulfate by Fe-Co layered doubled hydroxide for efficient catalytic degradation of Rhoadmine B, *Chemical Engineering Journal*, 2017, **321**, 222-232.
54. S. Huang, H. Wang, C. Xiang, D. Luo, H. Zeng, A. Cai, X. Ma, C. Fang and J. Deng, CoFe-prussian blue analogues@MXenes membrane activated peroxymonosulfate through enhanced electron transfer for nanoconfined catalytic degradation of bisphenol A: The crucial role of 1O2, *Journal of Membrane Science*, 2025, **719**.